



Article

Time-Dependent Density Functional Theory Calculations of N- and S-Doped TiO₂ Nanotube for Water-Splitting Applications

Yin-Pai Lin ¹, Inta Isakoviča ¹, Aleksejs Gopejenko ¹, Anna Ivanova ¹, Aleksandrs Začinskis ¹, Roberts I. Eglitis ¹, Pavel N. D'yachkov ² and Sergei Piskunov ^{1,*}

¹ Institute of Solid State Physics, University of Latvia, 8 Kengaraga Str., LV-1063 Riga, Latvia; in-bai.lin@cfi.lu.lv (Y.-P.L.); intai@cfi.lu.lv (I.I.); agopejen@cfi.lu.lv (A.G.); ann.che@cfi.lu.lv (A.I.); aleksandrs.zacinskis@cfi.lu.lv (A.Z.); rieglitis@cfi.lu.lv (R.I.E.)

² Kurnakov Institute of General and Inorganic Chemistry of the Russian Academy of Sciences, Leninskii Pr. 31, 119991 Moscow, Russia; p_dyachkov@rambler.ru

* Correspondence: piskunov@cfi.lu.lv

Abstract: On the basis of time-dependent density functional theory (TD-DFT) we performed first-principle calculations to predict optical properties and transition states of pristine, N- and S-doped, and N+S-codoped anatase TiO₂ nanotubes of 1 nm-diameter. The host O atoms of the pristine TiO₂ nanotube were substituted by N and S atoms to evaluate the influence of dopants on the photocatalytic properties of hollow titania nanostructures. The charge transition mechanism promoted by dopants positioned in the nanotube wall clearly demonstrates the constructive and destructive contributions to photoabsorption by means of calculated transition contribution maps. Based on the results of our calculations, we predict an increased visible-light-driven photoresponse in N- and S-doped and the N+S-codoped TiO₂ nanotubes, enhancing the efficiency of hydrogen production in water-splitting applications.

Keywords: TiO₂ nanotube; photocatalyst; time-dependent density functional theory; absorption spectra; transition contribution maps



Citation: Lin, Y.-P.; Isakoviča, I.; Gopejenko, A.; Ivanova, A.; Začinskis, A.; Eglitis, I.R.; D'yachkov, P.N.; Piskunov, S. Time-Dependent Density Functional Theory Calculations of N- and S-Doped TiO₂ Nanotube for Water-Splitting Applications. *Nanomaterials* **2021**, *11*, 2900. <https://doi.org/10.3390/nano11112900>

Academic Editor: Frederik Tielens

Received: 14 October 2021

Accepted: 26 October 2021

Published: 29 October 2021

Publisher's Note: MDPI stays neutral with regard to jurisdictional claims in published maps and institutional affiliations.



Copyright: © 2021 by the authors. Licensee MDPI, Basel, Switzerland. This article is an open access article distributed under the terms and conditions of the Creative Commons Attribution (CC BY) license (<https://creativecommons.org/licenses/by/4.0/>).

1. Introduction

Use of photodriven semiconductor-based catalyst is a promising route for energy production from sunlight. One of the main directions in this respect is utilization of the solar power for producing hydrogen fuel through the photocatalytic water-splitting reaction. Among all photocatalytic materials, titania (TiO₂) has been widely investigated since it was described for the first time by Fujishima and Honda [1]. The band gap width of TiO₂ (from 3.0 to 3.2 eV) allows efficient water-splitting under UV irradiation due to the positions of band edges—valence band maximum (VBM) of TiO₂ is located below the oxidation potential of water, while its conduction band minimum (CBM) is located above the proton reduction potential in many synthesized TiO₂-based compounds [2–12]. However, the relatively wide band gap of undoped TiO₂ leads to relatively poor efficiency of light absorption in the visible range of solar spectrum.

The total efficiency of the photocatalytic process strongly depends on charge transport and charge separation processes taking place in photocatalytic materials. In this respect, one-dimensional hollow nanostructures exhibit unique and advantageous features in comparison with three-dimensional and two-dimensional phases of photocatalytic materials [13]. However, the quantum confinement effect leads to a slightly increased band gap of nanotubes (NTs). To overcome these drawback, nonmetal dopants (such as N and S) have been proposed for TiO₂ NT to induce in-gap states allowing a visible-light-driven photoresponse suitable for water splitting [14,15].

Nowadays, with the tremendous revolution of computation techniques, theoretical calculations based on quantum-chemical methods have become a significant tool to in-

investigate photon-absorption mechanisms in solids. Density functional theory (DFT) and time-dependent density functional theory (TD-DFT) accompanied with the linear combination of atomic orbitals (LCAO) method allow the simulations of up to hundreds-atom structures and provide the reasonable equilibrium between accuracy, computational cost, and agreement with the experiment [16–25].

In this work, we focus on the theoretical predictions of electronic structure and optical properties of N- and S-doped TiO₂ NT. Calculations using both DFT and TD-DFT were performed to analyze the ground state, optical properties, absorption spectra, and to build the transition contribution maps (TCM) of doped TiO₂ NT. To predict the atomic composition of doped NT with the most-enhanced absorption properties, the following methodology is adopted: (i) calculations of electronic structure of N- and S-doped TiO₂ NT as a function of the dopant concentration; (ii) calculation of the absorption spectra and TCM to analyze the electron and hole transition mechanism in the doped NT; (iii) modeling of the N+S-codoped TiO₂ NT to combine the advantage of both N and S dopants to fulfill the criteria necessary for visible-light-driven photocatalytic water splitting.

2. Computational Details

Based on the equilibrium geometries of TiO₂ NT obtained using CRYSTAL17 package [26], the DFT and TD-DFT calculations were performed using the GPAW computer code [27,28] accompanied with ASE library [29]. Orbital configurations of the valence electrons were used as follows: O(2s²2p⁴), Ti(3s²3p⁶3d²4s²), N(2s²2p³), and S(3s²3p⁴). The default PAW dataset package 0.9.20000 and the double- ζ polarized (dzp) basis sets provided in GPAW package were utilized for all atoms consisting doped NT. Periodic boundary conditions were imposed along the x direction of the NT, while the vacuum gap of 15 Å width has been set along its y - z directions. The complete geometry optimization was performed using the Broyden–Fletcher–Goldfarb–Shanno (BFGS) algorithm. Calculations based on Perdew–Burke–Ernzerhof (PBE) exchange–correlation functional [30] within DFT were carried out to reach the equilibrium positions of all atoms comprising the NT. Optical properties of the relaxed TiO₂ NT with and without substitutional atoms (N, S) were calculated using the LCAO time propagation TD-DFT. To perform electronic band structure calculation, the Gritsenko–van Leeuwen–van Lenthe–Baerends functional with the solid-state modification (GLLB-SC) [31] was adopted due to its ability to describe reliably the band gap of TiO₂ [32].

In the ground state calculations at LCAO level of theory [33], the electronic structure of NTs was calculated using GLLB-SC functional and coarser grid of 0.25 Å. In order to perform the TD-DFT/LCAO time-propagation calculations necessary to obtain the optical absorption spectrum and TCM [16,34], our NT structures were evoked by weak δ -kick (dipole approximation) along z direction to simulate the incident light perpendicular to the nanotube wall. A semi-implicit Crank–Nicolson method was used to propagate the TD-DFT/LCAO [16,34]. The time-dependent dipole moments were imposed along the z axis to obtain the photoabsorption spectrum by means of Fourier transform [34]. The Gaussian (Lorentzian) spectral broadening with σ (η) corresponding to a full width at half-maximum (FWHM) has been used for time propagation [16,18,34]. In order to reduce the computational cost, the smallest length of the time-step and the total propagation time were adjusted according to the receipts given in Ref. [16]. The total propagation time used in this study was set to 500 time-steps of 20 attoseconds, each within the total propagation time of 10 femtoseconds. The photoabsorption spectra were calculated using the Lorentzian broadening function with $\eta = 0.07$ eV.

The complete photoabsorption spectrum $S(\omega)$ is composed from spectral constituents built from the Kohn–Sham decomposition of occupied states (electrons) to the unoccupied states (holes) $S_{occ}^{unocc}(\omega)$. In TCM, the ratio of $S_{occ}^{unocc}(\omega)$ and $S(\omega)$ is illustrated by scattering on Gaussian-broadened two-dimensional surface spanned by the density of states (DOS) drawn above (below) the Fermi level at the vertical and horizontal axes, respectively. The TCM is an illustrative data visualization to observe the superposition of multiple electron

and hole transitions for the photo-absorption at corresponding photon energy (wavelength, ω). The transition contribution are indicated by red (positive) and blue (negative) iso-lines. The positive (negative) transition contribution reveals the constructive (destructive) contribution of $S_{occ}^{unocc}(\omega)$ to the $S(\omega)$ (photoabsorption). For more details of LCAO time propagation in TD-DFT and TCM, please see Refs. [16–18,34,35]. VESTA software package [36] was used to visualize the atomic structure and positions of pseudowavefunction of NTs under study. Python packages NumPy [37] and Matplotlib [38] were utilized to analyze computed data and to produce the figures.

3. Results and Discussion

3.1. Pristine TiO₂ NT

Figure 1a,b illustrate the front and side projections of the studied NT. The unit cell of pristine anatase (8,0) TiO₂ (101) NT was periodically extended 4 times along the x axis. Thus, the NT model consists of 12 TiO₂ formula units or 96 atoms in total (Figure 1a). To fulfill the conditions for photocatalytic water splitting without the appliance of the external potential, two requirements have to be met [5,14]. The VBM of photocatalyst has to be smaller than the energy of thermodynamically favorable oxygen reduction reaction (-5.67 eV with respect to the vacuum level), while the CBM should be bigger than the energy of standard hydrogen electrode (SHE, -4.44 eV with respect to vacuum level). Figure 1c shows the projected density of states (PDOS) of pristine TiO₂ NT. The calculated band gap of the pristine TiO₂ NT is 3.257 eV, which is in a good agreement with the titania band gap of ~ 3 eV reported elsewhere [39–42]. The VBM and CBM positions of the pristine TiO₂ NT meet the criteria for water splitting under ultraviolet (UV) irradiation. To gain more insight about the utilization of solar light, the calculated absorption spectrum of pristine TiO₂ NT is shown in Figure 1d. The wide band gap of the TiO₂ NT restricts the efficiency of solar light absorption as only about four percent of the solar spectrum falls in the UV range. In our previous study on N- and S-doped TiO₂ NT [15], we predict an obvious blueshift of the imaginary part of the dielectric function. As it is reported in the literature, the absorption spectrum of TiO₂ NT can be slightly blueshifted in comparison with TiO₂ thin films [39] and powders [40]. The blueshift of the absorption spectrum is well pronounced for the pristine TiO₂ NT.

Our group has previously studied the anatase (n,0) TiO₂ (001) NT and anatase (0,n) TiO₂ (101) NTs [13–15,43] by means of ground state total energy calculations. In this work, the pristine TiO₂ NT is rolled up from the anatase TiO₂ (101) 6-layered slab. The aim of the current study is to understand the influence of substitutional N and S atoms replacing the host oxygens on the improvement of band edge positions in view of enhancement in light absorption. We note that the NT modeled in this study can hardly be synthesized. However, concerning the balance between convergence criteria and structure stability, the elaborated model presents most of the features arising from the substitutional atoms at low computational cost. Our strategy for prediction of the most photocatalytically efficient doped TiO₂ NT material can be summarized as follows: (i) The VBM and CBM must meet the conditions for water splitting ($\text{VBM} < \text{O}_2/\text{H}_2\text{O} < \text{H}^+/\text{H}_2 < \text{CBM}$); (ii) doped TiO₂ NT has to be able to absorb maximum photons from solar irradiation in visible range. The absorption spectrum calculated for nanostructures under study is expected to be redshifted and demonstrate obvious enhancement. The mechanism of absorption is represented by calculated TCMs to provide a deeper understanding of electron and hole transition of involved substitutional atoms.

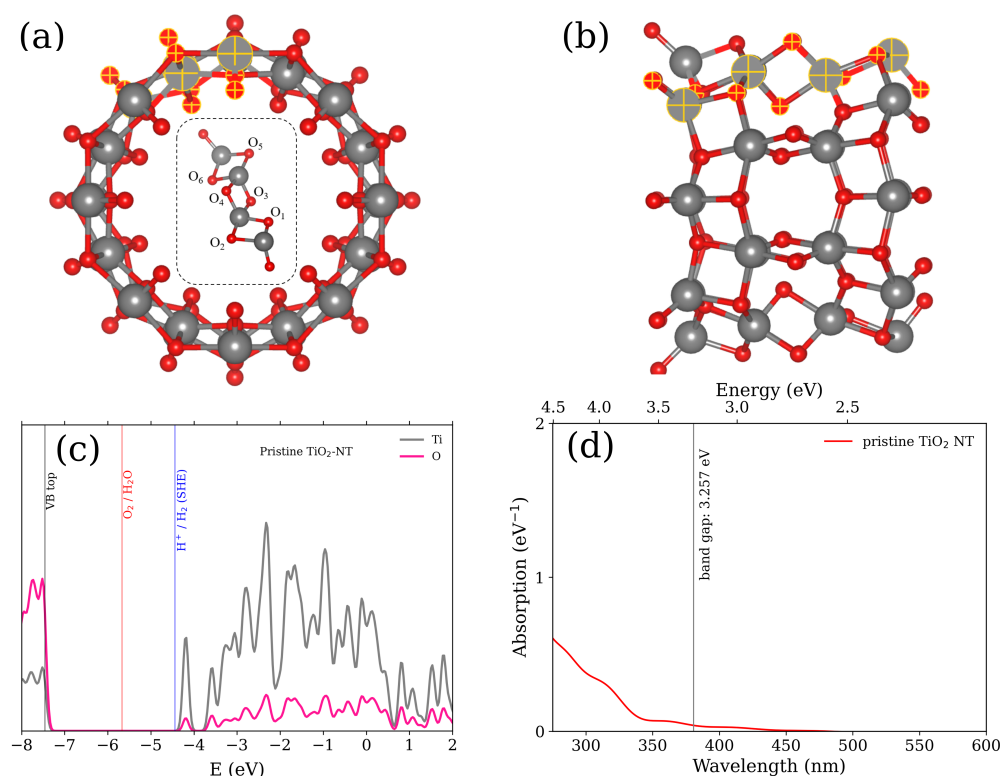


Figure 1. Schematic illustration of the pristine (8,0) anatase (101) TiO_2 NT with the diameter of 0.933 nm: (a) front view of the NT, and (b) side view of the NT. Ti atoms are shown as gray balls, oxygens are shown as red balls. The inset in (a) shows the unit cell of the TiO_2 NT repeated 8 times by rototranslational symmetry. The numbered O atoms denote the doping sites. (c) The projected density of states (PDOS) of pristine TiO_2 NT as calculated by means of GLLB-SC exchange–correlation functional within DFT. Vertical black line crossing the DOS plot corresponds to VBM of the pristine TiO_2 NT, while red and blue lines correspond to $\text{O}_2/\text{H}_2\text{O}$ and H^+/H_2 redox potentials with respect to the vacuum level, respectively. (d) is the calculated optical absorption spectrum of the pristine TiO_2 NT. Vertical black line crossing the spectrum corresponds to the band gap width of the pristine TiO_2 NT.

3.2. N- and S-Doped TiO_2 NT

3.2.1. Ground State

In this work, two cases of the doped TiO_2 NT are considered. In the first case, the substitutional N or S atoms in the periodically repeated unit (inset in the Figure 1a) are replicated along the whole NT wall. As the unit cell of nanotube NT is repeated by 8 rototranslational symmetry operators (i.e., rotation axis is of 8th order), the total number of substitutional atoms is therefore equal to eight. All such dopant combinations are marked as 8N/ TiO_2 NT and 8S/ TiO_2 NT, respectively. In the second case, only one N or S atom replaces the numbered oxygen atom in the whole NT wall. These combinations are marked as 1N/ TiO_2 NT and 1S/ TiO_2 NT, respectively. Substitutional N and S atoms sequentially replace the numbered host oxygen atoms in six positions depicted in the inset in Figure 1a. Figure 2 shows the projected density of states (PDOS) calculated for the 24 substitutional configurations of the doped TiO_2 NT. In total, the S-doped TiO_2 NT shows a more general improvement of the band gap width for both 8S/ TiO_2 NT and 1S/ TiO_2 NT. According to the electronic configuration of the S dopant, extra electrons contribute to the mid-gap states of the S-doped TiO_2 NT. As for the N-doped TiO_2 NT, most of the induced states are gathered in the vicinity of the VBM of TiO_2 NT. Only few configurations can therefore correspond to the relatively isolated mid-gap states (Figure 2i,k).

Calculated PDOSs prove that the doped atoms on the inner surface of NT wall (O_1 , O_3 , and O_5) have more influence on the electronic structure due to the distance between the dopant and neighboring host atoms. One of the most apparent cases is the 8S/ TiO_2 at O_3 position in Figure 2j. In this case, the doped S atoms not only improve the band gap,

but also induce a series of mid-gap states. Taking into account the band gap width, S and N dopants placed at the O₃ position is a suitable choice to overcome the UV drawback of the pristine TiO₂ NT. However, dopants placed on the inner surface of the NT wall cause another problem in light of photocatalytic water splitting. Based on the criteria for efficient water splitting, the VBM should be placed below the O₂/H₂O potential. This requirement is not fulfilled for five dopant positions, as shown in Figure 2d,i,j,l,t. The common point of these five cases is that the positions of the numbered oxygen atoms are located on the inner side of the TiO₂ NT wall. Although the concentration of dopants can tune the energy of VBM, this approach is not feasible for the positions shown in Figure 2j,l. In contrast, the doped atoms on the outer surface of the NT wall (O₂, O₄, and O₆) meet all conditions for photocatalytic water splitting. Summing up, doping pristine TiO₂ NT with N and S improves the VBM and CBM of the band gap; however, the positions of the substitutional atoms play a significant role in meeting the condition of efficient photocatalytic water splitting.

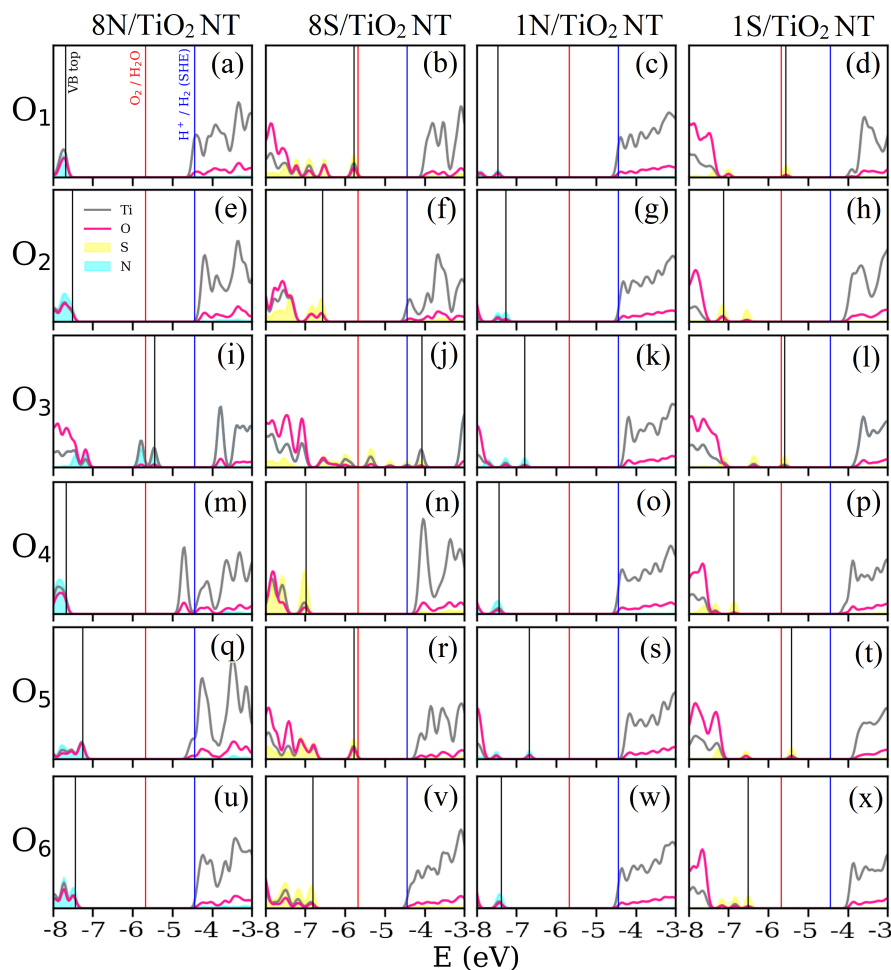


Figure 2. Projected density of states (PDOS) of the N- (cyan) or S- (yellow) doped TiO₂ NT. Each row corresponds to the numbered host oxygens substituted by dopant (O₁ to O₆); each column represents the total number of doped atoms (8N, 8S, 1N, 1S). (a) 8N/TiO₂ NT at O₁; (b) 8S/TiO₂ NT at O₁; (c) 1N/TiO₂ NT at O₁; (d) 1S/TiO₂ NT at O₁; (e) 8N/TiO₂ NT at O₂; (f) 8S/TiO₂ NT at O₂; (g) 1N/TiO₂ NT at O₂; (h) 1S/TiO₂ NT at O₂; (i) 8N/TiO₂ NT at O₃; (j) 8S/TiO₂ NT at O₃; (k) 1N/TiO₂ NT at O₃; (l) 1S/TiO₂ NT at O₃; (m) 8N/TiO₂ NT at O₄; (n) 8S/TiO₂ NT at O₄; (o) 1N/TiO₂ NT at O₄; (p) 1S/TiO₂ NT at O₄; (q) 8N/TiO₂ NT at O₅; (r) 8S/TiO₂ NT at O₅; (s) 1N/TiO₂ NT at O₅; (t) 1S/TiO₂ NT at O₅; (u) 8N/TiO₂ NT at O₆; (v) 8S/TiO₂ NT at O₆; (w) 1N/TiO₂ NT at O₆; (x) 1S/TiO₂ NT at O₆. Vertical lines crossing all the DOS plots correspond to VBM of the doped TiO₂ NT (black), while red lines and blue lines correspond to the O₂/H₂O and H⁺/H₂ redox potentials positioned with respect to the vacuum level, respectively. The PDOS peaks of dopants are scaled by the factor of two.

3.2.2. Optical Property

To study the influence of N and S dopants on optical photoresponse of the TiO₂ NT, in Figure 3, we illustrate the enhancement due to the redshift in optical absorption spectra calculated for the most promising doping scenarios obtained from the ground state calculations shown in Figure 2. The dopants positioned on the inner surface of the NT wall cause strong photon absorption for both N- and S-doped TiO₂ NTs. This is an influence of apparent mid-gap states located between the VBM and CBM. For example, the 8S/TiO₂ NT doped at O₃ position shows the most enhanced absorption as the photon energy is below the band gap of pristine TiO₂ NT. This phenomena is observed even if dopant concentration decreases. For the 1S/TiO₂ and 1N/TiO₂ NT cases doped at O₃ position, the absorption is yet to be enhanced. We note that the most obvious photoenhancement and the most pronounced redshift in the calculated absorption spectra depends not only on the positions of dopant, but also can be triggered by the interband transitions at lower energy. The dopants positioned at outer surface of the TiO₂ NT wall form more concentrated states in the vicinity of VBM of the pristine TiO₂ NT. In spite of the fact that the mid-gap states have tremendous effect on the improvement of the band gap width, they do not always contribute to the enhancement of the optical absorption spectra.

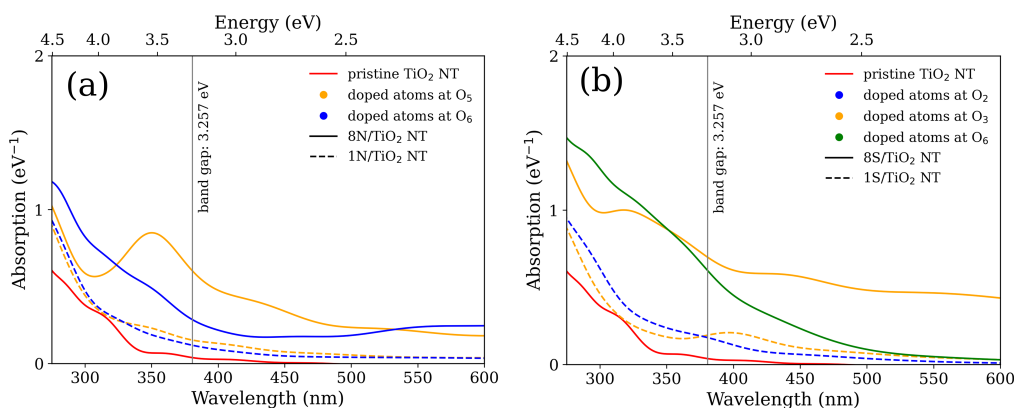


Figure 3. Absorption spectra of (a) N- and (b) S-doped TiO₂ NTs. The red line is the absorption spectrum of the pristine TiO₂ NT. The solid lines correspond to the 8N/TiO₂- and 8S/TiO₂-doped scenario (Figure 2), while the dashed lines are for the single atom doped NTs. For N-doped TiO₂ NTs (a): the orange color is for the dopant placed at the O₅ position and the blue color is for the dopant placed at the O₆ position. For S-doped TiO₂ NTs (b): the orange color is for the dopant placed at O₃ position; the blue color is for the dopant placed at O₂ position; and the green color is for the dopant placed at O₆ position. The orange color is for the dopants placed on the inner surface of the NT wall. The blue and green color are for the dopants placed on the outer surface of the NT wall. The position of O_{*n*} is related to the inset of Figure 1a.

To predict the charge transitions induced by dopants that are placed on both the inner and outer surfaces of NT wall, the calculated TCMs for the electron-hole transitions between occupied and unoccupied states at certain energies (wavelengths) are shown in Figure 4. To be more specific, we focus on the 8N/TiO₂ NT and 8S/TiO₂ NT doping scenarios to emphasize the transitions at the abundant N or S states. Energy of 4.0 eV with respect to the vacuum level was chosen to elucidate the mechanism of transition and to demonstrate an enhancement of the light absorption if the dopants are placed at outer NT surface. For the N-doped TiO₂ NT, it is clear that the dopant placed at inner surface of the TiO₂ NT has a negative contribution to absorption, as shown in Figure 4a. In contrast, there is no negative contribution if dopant is placed at outer surface of the TiO₂ NT wall, as it is shown in Figure 4b. For the S-doped TiO₂ NT, both the dopant placed at inner and outer surfaces of the TiO₂ NT wall demonstrate the negative contribution. However, the apparent states gathering around the VBM provide strong positive contribution neglecting the negative part.

From the calculated absorption properties, we can conclude that the mid-gap states positioned between the VBM and the CBM of the pristine TiO₂ NT can actually improve the

visible-light-driven photoabsorption. In our model, the dopant placed on the inner surface of the TiO₂ NT results in the emerging of mid-gap states responsible for the enhanced photoresponse. Our calculations predict that the S-doped titania NT is more promising than the N-doped NT. However, the advantage of defect-induced mid-gap states may not be as attractive considering all the criteria necessary for efficient photocatalytic water splitting. In some doping scenarios, the mid-gap states greatly improving the band gap width do not meet the redox potential condition, i.e., the VBM is bigger than the energy potential of the oxygen reduction reaction or the mid-gap states lead to the negative contribution above the band gap energy. On the other hand, the dopants placed on the outer surface of NT wall with just a few mid-gap states reveal more pronounced redshift at the higher energy.

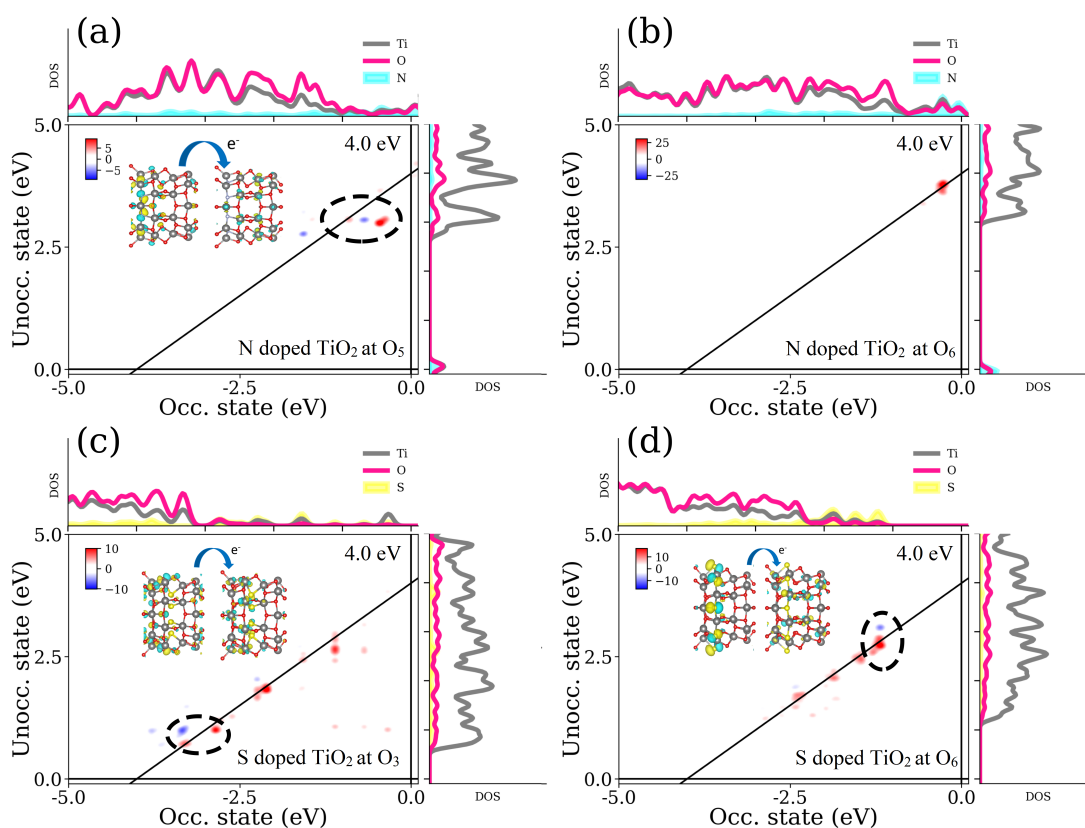


Figure 4. Transition contribution maps (TCM) of N- and S-doped TiO₂ NT. (a) N-doped TiO₂ NT at O₅; (b) N-doped TiO₂ NT at O₆; (c) S-doped TiO₂ NT at O₃; (d) S-doped TiO₂ NT at O₆. The diagonal solid-lines are used to emphasize the constant transition energy of 4.0 eV. DOS includes Ti (grey), O (pink), and dopants (N—cyan and S—yellow) projections. The insets show that orbitals contributed to negative transition (marked by ellipse). The reference energy is set to the Fermi level of each nanostructure separately. Below the Fermi level are occupied states; above the Fermi level are unoccupied states. The color scheme set to elucidate the positive (red) and negative (blue) transition contributions. The color intensity is the ratio between $S_{occ}^{unocc.}(\omega)$ and $S(\omega)$.

3.3. N+S-Codoped TiO₂ NT

Motivated by the promising results obtained for N- and S-doped NT, we modeled the N+S-codoped TiO₂ NT to estimate the most enhanced absorption spectra under the condition necessary for efficient visible-light-driven water splitting. Figure 5 presents the absorption spectra (Figure 5a), calculated PDOS for the 8N+8S/TiO₂ NT (Figure 5b), and calculated PDOS for the 1N+1S/TiO₂ NT (Figure 5c). For the 8N+8S/TiO₂-doped NT, atomic structure is as follows: the N dopants are placed at O₆ positions, while the S dopants are placed at O₄ positions. The band gap of 8N+8S/TiO₂-doped NT is 2.798 eV. The CBM of 8N+8S/TiO₂ NT is located at −4.53 eV, which is slightly below SHE equilibrium

potential (-4.44 eV). As for the 1N+1S/TiO₂-doped NT, its atomic structure consists of the N dopant placed at O₄ positions, while the S dopant substitutes host oxygen at O₃ positions opposite to the N dopant. The band gap of 1N+1S/TiO₂-doped NT is equal to 1.719 eV. We note that the 1S/TiO₂-doped NT at O₃ position would cause the VBM above the level of equilibrium oxygen reduction reaction potential. Doping of the TiO₂ NT with an additional N atom at the suitable position leads not only to the adjustment of the band gap width of the S-doped TiO₂ NT, but also restrains the VBM below the redox levels necessary for water splitting. As can be seen from the calculated absorption spectra in Figure 5a, the redshift is well pronounced. The redshift of absorption spectrum means an increase in electron–hole pairs of doped TiO₂ NT being involving in the charge transition. In Figure 5a, absorption begins at energies around 3.65 eV (red circle), 3.45 eV (blue circle), and 2.7 eV (orange circle) depicted for pristine TiO₂ NT, 1N+1S/TiO₂ codoped NT, and 8N+8S/TiO₂ codoped NT, respectively. The induced states in the vicinity of the VBM of the pristine TiO₂ NT indicate the enhanced interband transition necessary for the increased visible-light-driven photoresponse.

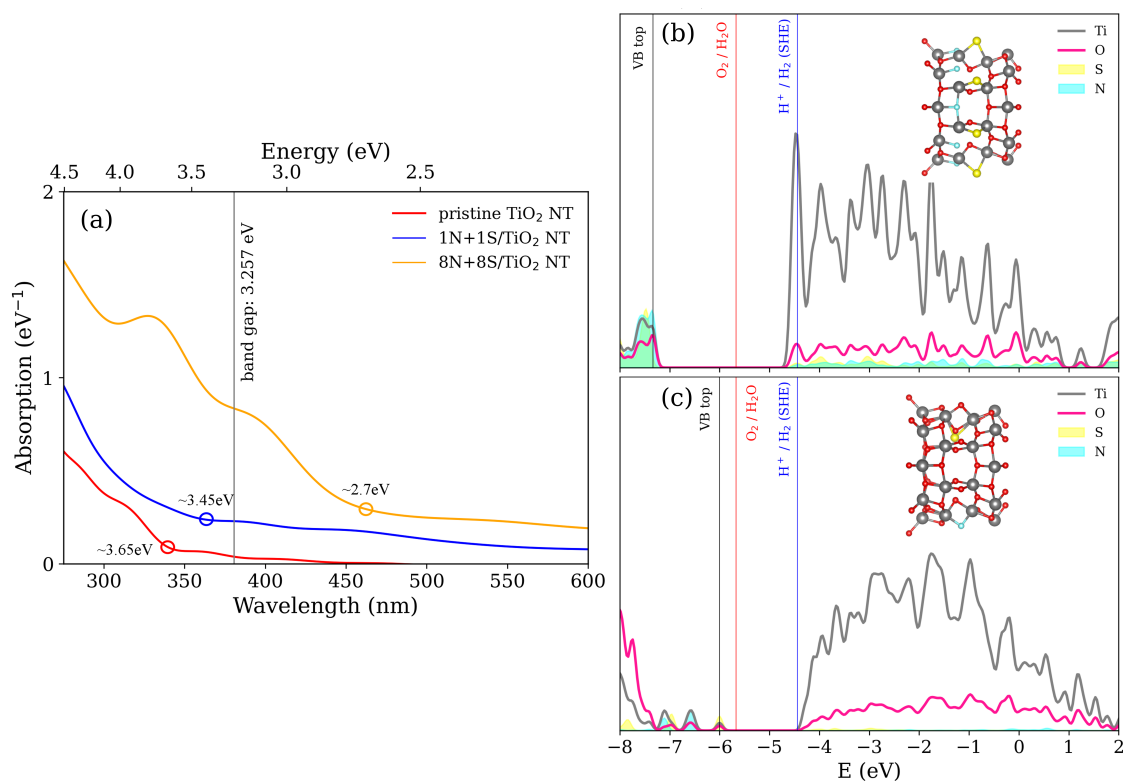


Figure 5. Absorption spectra and calculated projected density of states (PDOS) of N+S-codoped TiO₂ NT. (a) absorption spectra include pristine TiO₂ NT, 8N+8S/TiO₂ doped NT, and 1N+1S/TiO₂ doped NT. (b) PDOS for the 8N+8S/TiO₂ NT and (c) for the 1N+1S/TiO₂ NT. The insets show the equilibrium atomic structures for each model in consideration.

4. Conclusions

In this study, we demonstrated that the combination of N and S dopants replacing the host oxygen atoms in TiO₂ NT can enhance the visible-light-driven photoresponse and cause redshift of TiO₂ NT absorption spectra under the conditions necessary for water splitting. We calculated the electronic and optical properties of N- and S-doped TiO₂ NTs, taking into account the high and low dopant ratios by means of DFT and TD-DFT. From our calculations, we can conclude that the shorter the bond length between the dopant and neighbored host atoms, the larger the number of mid-gap states induced. The strong interaction between the dopants and neighboring host atoms leads to the VBM of the doped TiO₂ NT positioned above the oxygen redox potential, while the abundant states of

doped TiO₂ NT are involved in charge transition. These states tend to form the destructive contribution of electron and hole transition at higher energy. We suggest possible scenarios for enhancing the optical absorption of the doped titania NTs allowing for the obvious enhancement and redshift of calculated absorption spectra of doped TiO₂ NT depending on dopant concentration. Based on our theoretical calculation, we predict that the use of an N+S-codoped TiO₂ NT catalyst could increase the efficiency of visible-light-driven photocatalytic water-splitting applications.

Author Contributions: Conceptualization, Y.-P.L., P.N.D., S.P. and R.I.E.; methodology, Y.-P.L. and S.P.; software, Y.-P.L.; validation, Y.-P.L. and S.P.; formal analysis, Y.P.L., A.G., A.I., A.Z., S.P. and R.I.E.; investigation, Y.-P.L.; resources, S.P.; data curation, Y.-P.L. and S.P.; writing—original draft preparation, Y.-P.L., I.I., A.G., A.Z., and S.P.; writing—review and editing, Y.-P.L., A.I., A.G., A.Z., P.N.D., S.P. and R.I.E.; visualization, Y.-P.L.; supervision, S.P.; project administration, I.I. and S.P.; funding acquisition, S.P. All authors have read and agreed to the published version of the manuscript.

Funding: This research was funded by the Latvian Scientific Council grant LZP-2018/2-0083. Institute of Solid State Physics, University of Latvia, as the Center of Excellence, has received funding from the European Union's Horizon 2020 Framework Program H2020-WIDESPREAD-01-2016-2017-TeamingPhase2 under Grant Agreement No. 739508, project CAMART².

Data Availability Statement: The raw/processed data required to reproduce these findings cannot be shared at this time as the data also form a part of an ongoing study.

Conflicts of Interest: The authors declare no conflict of interest. The funders had no role in the design of the study; in the collection, analyses, or interpretation of data; in the writing of the manuscript, or in the decision to publish the results.

References

1. Fujishima, A.; Honda, K. Electrochemical photolysis of water at a semiconductor electrode. *Nature* **1972**, *238*, 37–38. [[CrossRef](#)]
2. Maeda, K. Photocatalytic Water Splitting Using Semiconductor Particles: History and Recent Developments. *J. Photochem. Photobiol. C* **2011**, *12*, 237–268. [[CrossRef](#)]
3. Li, B.; Wu, S.; Gao, X. Theoretical calculation of a TiO₂-based photocatalyst in the field of water splitting: A review. *Nanotechnol. Rev.* **2020**, *9*, 1080–1103. [[CrossRef](#)]
4. Razek, S.; Popeil, M.; Wangoh, L.; Rana, J.; Suwandaratne, N.; Andrews, J.; Watson, D.; Banerjee, S.; Piper, L. Designing catalysts for water splitting based on electronic structure considerations. *Electron. Struct.* **2020**, *2*, 023001. [[CrossRef](#)]
5. Catlow, C.R.A.; Guo, Z.X.; Miskufova, M.; Shevlin, S.A.; Smith, A.G.H.; Sokol, A.A.; Walsh, A.; Wilson, D.J.; Woodley, S.M. Advances in computational studies of energy materials. *Philos. Trans. R. Soc. A Math. Phys. Eng. Sci.* **2010**, *368*, 3379–3456. [[CrossRef](#)]
6. Serga, V.; Burve, R.; Krumina, A.; Romanova, M.; Kotomin, E.A.; Popov, A.I. Extraction-Pyrolytic Method for TiO₂ Polymorphs Production. *Crystals* **2021**, *11*, 431. [[CrossRef](#)]
7. Tsebriienko, T.; Popov, A.I. Effect of Poly(Titanium Oxide) on the Viscoelastic and Thermophysical Properties of Interpenetrating Polymer Networks. *Crystals* **2021**, *11*, 794. [[CrossRef](#)]
8. Serga, V.; Burve, R.; Krumina, A.; Pankratova, V.; Popov, A.I.; Pankratov, V. Study of phase composition, photocatalytic activity, and photoluminescence of TiO₂ with Eu additive produced by the extraction-pyrolytic method. *J. Mater. Res. Technol.* **2021**, *13*, 2350–2360. [[CrossRef](#)]
9. Dukenbayev, K.; Kozlovskiy, A.; Kenzhina, I.; Berguzinov, A.; Zdorovets, M. Study of the effect of irradiation with Fe⁷⁺ ions on the structural properties of thin TiO₂ foils. *Mater. Res. Express* **2019**, *6*, 046309. [[CrossRef](#)]
10. Kozlovskiy, A.; Shlimas, D.; Kenzhina, I.; Boretskiy, O.; Zdorovets, M. Study of the Effect of Low-Energy Irradiation with O²⁺ Ions on Radiation Hardening and Modification of the Properties of Thin TiO₂ Films. *J. Inorg. Organomet. Polym. Mater.* **2021**, *31*, 790–801. [[CrossRef](#)]
11. Osinkin, D.A.; Antonova, E.P.; Lesnichyova, A.S.; Tropin, E.S.; Chernov, M.E.; Chernov, E.I.; Farlenkov, A.S.; Khodimchuk, A.V.; Eremin, V.A.; Kovrova, A.I.; et al. Application of Promising Electrode Materials in Contact with a Thin-Layer ZrO₂-Based Supporting Electrolyte for Solid Oxide Fuel Cells. *Energies* **2020**, *13*, 1190. [[CrossRef](#)]
12. Osinkin, D.A.; Khodimchuk, A.V.; Porotnikova, N.M.; Bogdanovich, N.M.; Fetisov, A.V.; Ananyev, M.V. Rate-Determining Steps of Oxygen Surface Exchange Kinetics on Sr₂Fe_{1.5}Mo_{0.5}O_{6-δ}. *Energies* **2020**, *13*, 250. [[CrossRef](#)]
13. Lisovski, O.; Piskunov, S.; Bocharov, D.; Kenmoe, S. 2D slab models of TiO₂ nanotubes for simulation of water adsorption: Validation over a diameter range. *Results Phys.* **2020**, *19*, 103527. [[CrossRef](#)]
14. Piskunov, S.; Lisovski, O.; Begens, J.; Bocharov, D.; Zhukovskii, Y.F.; Wessel, M.; Spohr, E. C-, N-, S-, and Fe-Doped TiO₂ and SrTiO₃ Nanotubes for Visible-Light-Driven Photocatalytic Water Splitting: Prediction from First Principles. *J. Phys. Chem. C* **2015**, *119*, 18686–18696. [[CrossRef](#)]

15. Kenmoe, S.; Lisovski, O.; Piskunov, S.; Zhukovskii, Y.F.; Spohr, E. Electronic and optical properties of pristine, N- and S-doped water-covered TiO₂ nanotube surfaces. *J. Chem. Phys.* **2019**, *150*, 041714. [[CrossRef](#)] [[PubMed](#)]
16. Rossi, T.; Kuisma, M.; Puska, M.; Nieminen, R.; Erhart, P. Kohn-Sham decomposition in real-time time-dependent density-functional theory: An efficient tool for analyzing plasmonic excitations. *J. Chem. Theory Comput.* **2017**, *13*, 4779–4790. [[CrossRef](#)] [[PubMed](#)]
17. Conley, K.; Nayyar, N.; Rossi, T.; Kuisma, M.; Turkowski, V.; Puska, M.; Rahman, T. Plasmon excitations in mixed metallic nanoarrays. *ACS Nano* **2019**, *13*, 5344–5355. [[CrossRef](#)]
18. Rossi, T.; Shegai, T.; Erhart, P.; Antosiewicz, T. Strong plasmon-molecule coupling at the nanoscale revealed by first-principles modeling. *Nat. Commun.* **2019**, *10*, 3336. [[CrossRef](#)]
19. Zhukovskii, Y.F.; Pugno, N.; Popov, A.I.; Balasubramanian, C.; Bellucci, S. Influence of F centres on structural and electronic properties of AlN single-walled nanotubes. *J. Phys. Condens. Matter* **2007**, *19*, 395021. [[CrossRef](#)]
20. Bellucci, S.; Popov, A.I.; Balasubramanian, C.; Cinque, G.; Marcelli, A.; Karbovnyk, I.; Savchyn, V.; Krutyak, N. Luminescence, vibrational and XANES studies of AlN nanomaterials. *Radiat. Meas.* **2007**, *42*, 708–711. [[CrossRef](#)]
21. Kamenov, V.; Hu, Y.; Shamonina, E.; Ringhofer, K.; Gayvoronsky, V.Y. Two-wave mixing in (111)-cut Bi₁₂SiO₂₀ and Bi₁₂TiO₂₀ crystals: Characterization and comparison with the general orientation. *Phys. Rev. E* **2000**, *62*, 2863. [[CrossRef](#)] [[PubMed](#)]
22. Frejlich, J.; Freschi, A.; Garcia, P.; Shamonina, E.; Gayvoronsky, V.Y.; Ringhofer, K. Feedback-controlled running holograms in strongly absorbing photorefractive materials. *JOSA B* **2000**, *17*, 1517–1521. [[CrossRef](#)]
23. Bellucci, S.; Balasubramanian, C.; Ivanov, A.; Popov, A.; Schober, H. Neutron characterization of aluminium nitride nanotubes. *J. Neutron Res.* **2006**, *14*, 287–291. [[CrossRef](#)]
24. Karbovnyk, I.; Klym, H.; Piskunov, S.; Popov, A.; Chalyy, D.; Zhydenko, I.; Lukashevych, D. The impact of temperature on electrical properties of polymer-based nanocomposites. *Low Temp. Phys.* **2020**, *46*, 1231–1234. [[CrossRef](#)]
25. Chuklina, N.; Piskunov, S.; Popov, N.; Mysovsky, A.; Popov, A. Comparative quantum chemistry study of the F-center in lanthanum trifluoride. *Nucl. Instrum. Methods Phys. Res. B* **2020**, *474*, 57–62. [[CrossRef](#)]
26. Dovesi, R.; Erba, A.; Orlando, R.; Zicovich-Wilson, C.M.; Civalieri, B.; Maschio, L.; Rérat, M.; Casassa, S.; Baima, J.; Salustro, S.; et al. Quantum-mechanical condensed matter simulations with CRYSTAL. *Wiley Interdiscip. Rev. Comput. Mol. Sci.* **2018**, *8*, e1360. [[CrossRef](#)]
27. Enkovaara, J.; Rostgaard, C.; Mortensen, J.J.; Chen, J.; Dulak, M.; Ferrighi, L.; Gavnholt, J.; Glinsvad, C.; Haikola, V.; Hansen, H.A.; et al. Electronic structure calculations with gpaw: A real-space implementation of the projector augmented-wave method. *J. Phys. Condens. Matter* **2010**, *22*, 253202:1–253202:24. [[CrossRef](#)]
28. Walter, M.; Häkkinen, H.; Lehtovaara, L.; Puska, M.; Enkovaara, J.; Rostgaard, C.; Mortensen, J. Time-dependent density-functional theory in the projector augmented-wave method. *J. Chem. Phys.* **2008**, *128*, 244101. [[CrossRef](#)] [[PubMed](#)]
29. Larsen, A.H.; Mortensen, J.J.; Blomqvist, J.; Castelli, I.E.; Christensen, R.; Dulak, M.; Friis, J.; Groves, M.N.; Hammer, B.; Hargus, C.; et al. The atomic simulation environment—A Python library for working with atoms. *J. Phys. Condens. Matter* **2017**, *29*, 273002. [[CrossRef](#)]
30. Perdew, J.P.; Burke, K.; Ernzerhof, M. Generalized Gradient Approximation Made Simple. *Phys. Rev. Lett.* **1997**, *77*, 3865–3868. [[CrossRef](#)]
31. Kuisma, M.; Ojanen, J.; Enkovaara, J.; Rantala, T.T. Kohn-Sham potential with discontinuity for band gap materials. *Phys. Rev. B* **2010**, *82*, 115106. [[CrossRef](#)]
32. Hastrup, S.; Strange, M.; Pandey, M.; Deilmann, T.; Schmidt, P.S.; Hinsche, N.F.; Gjerding, M.N.; Torelli, D.; Larsen, P.M.; Riis-Jensen, A.C.; et al. The computational 2D materials database: High-throughput modeling and discovery of atomically thin crystals. *2D Mater.* **2018**, *5*, 042002. [[CrossRef](#)]
33. Larsen, A.H.; Vanin, M.; Mortensen, J.J.; Thygesen, K.S.; Jacobsen, K.W. Localized atomic basis set in the projector augmented wave method. *Phys. Rev. B* **2009**, *80*, 195112. [[CrossRef](#)]
34. Kuisma, M.; Sakko, A.; Rossi, T.; Larsen, A.H.; Enkovaara, J.; Lehtovaara, L.; Rantala, T.T. Localized surface plasmon resonance in silver nanoparticles: Atomistic first-principles time-dependent density-functional theory calculations. *Phys. Rev. B* **2015**, *91*, 115431. [[CrossRef](#)]
35. Mokka, J.H. Strong Collectivity of Optical Transitions in Lead Halide Perovskite Quantum Dots. *Plasmonics* **2020**, *15*, 581–590. [[CrossRef](#)]
36. Momma, K.; Izumi, F. VESTA 3 for three-dimensional visualization of crystal, volumetric and morphology data. *J. Appl. Cryst.* **2011**, *44*, 1272–1276. [[CrossRef](#)]
37. Van der Walt, S.; Colbert, S.C.; Varoquaux, G. The numpy array: A structure for efficient numerical computation. *Comput. Sci. Eng.* **2011**, *13*, 22–30. [[CrossRef](#)]
38. Hunter, J.D. Matplotlib: A 2D graphics environment. *Comput. Sci. Eng.* **2007**, *9*, 90–95. [[CrossRef](#)]
39. Wang, W.; Wang, Z.; Liu, J.; Luo, Z.; Suib, S.L.; He, P.; Ding, G.; Zhang, Z.; Sun, L. Single step one-pot synthesis of TiOS nanosheets doped with sulfur on reduced graphene oxide with enhanced photocatalytic activity. *Sci. Rep.* **2017**, *7*, 446610.
40. Xu, J.; Wang, F.; Liu, W.; Cao, W. Nanocrystalline n-doped TiO₂ powders: mild hydrothermal synthesis and photocatalytic degradation of phenol under visible light irradiation. *Int. J. Photoenergy* **2013**, *2013*, 616139.
41. Seo, S.-H.; Kim, B.-I. Effect of Cu, Cr, S Doped TiO₂ for Transparent Plastic Bar Reinforced Concrete. *Appl. Sci.* **2020**, *10*, 7334. [[CrossRef](#)]

-
42. Wu, Y.; Mu, H.; Cao, X.; He, X. Polymer-supported graphene-TiO₂ doped with nonmetallic elements with enhanced photocatalytic reaction under visible light. *J. Mater. Sci.* **2020**, *55*, 1577–1591. [[CrossRef](#)]
 43. Lisovski, O.; Piskunov, S.; Bocharov, D.; Kenmoe, S. 2D Slab Models of Nanotubes Based on Tetragonal TiO₂ Structures: Validation over a Diameter Range. *Nanomaterials* **2021**, *11*, 1925. [[CrossRef](#)]